



Magnetron sputtered high entropy alloy/amorphous carbon nanocomposite coatings

León Zendejas Medina^{a,*}, Marcus Vinícius Tavares de Costa^b, Olivier Donzel-Gargand^c,
Leif Nyholm^a, E. Kristofer Gamstedt^d, Ulf Jansson^a

^a Uppsala University, Department of Chemistry – Ångström Laboratory, SE-751 21 Uppsala, Sweden

^b Karlstad University, Department of Engineering and Chemical Sciences, SE-651 88 Karlstad, Sweden

^c Uppsala University, Division of Solar Cell Technology, Department of Materials Science and Engineering, SE-75121 Uppsala, Sweden

^d Uppsala University, Division of Applied Mechanics, Department of Materials Science and Engineering, SE-751 21 Uppsala, Sweden

ARTICLE INFO

Keywords:

Magnetron sputtering
Nanocomposite
Amorphous carbon
Fragmentation test

ABSTRACT

Magnetron sputter deposition of metal/carbon nanocomposites has been explored for many metals and a few alloys. In this paper, the formation of nanocomposites based on complex high entropy alloys (HEAs) was explored, focusing on the effect of the average carbon affinity on the phase formation. Two HEA systems were compared: CoCrFeMnNi and Cr₂₆Fe₂₇Ni₂₇Ta₂₀. For each alloy, around 20–50 at% carbon was added through combinatorial co-sputtering. Thermodynamic calculations predicted decomposition of these materials into multiple alloy phases, metal carbides, and, at higher concentrations, free graphitic carbon. Free carbon was found in the coatings at carbon concentrations above 28 and 33 at% for the CoCrFeMnNi and Cr₂₆Fe₂₇Ni₂₇Ta₂₀ systems, respectively, which agreed with the theoretical predictions. However, the segregation of metallic elements and the formation of crystalline carbides were suppressed by the rapid quenching during deposition. All coatings were, instead, amorphous and consisted of either a single metallic phase or a mixture of a metallic phase and sp²- and sp³-hybridized carbon. Mechanical and electrochemical tests were performed, including in-situ fragmentation tests to quantify the crack resistance. The presence of free carbon made the coatings softer than the corresponding single-phase materials. Under tensile strain, the nanocomposite coatings formed a larger number of narrower cracks and exhibited less delamination at high strains.

1. Introduction

Magnetron sputtered transition metal (TM)/carbon nanocomposites with metallic grains in a free carbon matrix have been widely studied in the literature [1–3]. The phase formation of such coatings is strongly dependent on the carbide-forming ability of the metals. All metals can dissolve a small amount of carbon interstitially. When the carbon solubility is surpassed, the phase evolution follows different paths depending on the carbon affinity. Elements with high carbon affinities typically form a single metal carbide phase. This is the case for the transition metals (TMs) in Group 4 and Group 5 of the periodic system. Their carbides have a simple NaCl structure and are thus easily formed during sputter deposition [4]. When no more carbon can be added to the carbide phase, an amorphous carbon phase (a-C) appears [5,6]. Weak carbide-forming metals, such as Fe and Ni, have a different phase evolution. After the initial interstitial solubility, they first form amorphous

carbon-containing alloys, followed by a mixture of an amorphous metal-containing phase and a-C [7,8]. The presence of a-C is found at lower carbon contents compared to the stronger carbide formers. Cr is an intermediate case; it can form stable carbides (Cr₂₃C₆, Cr₇C₃, and Cr₃C₂) but with more complex structures and lower carbon contents than the TMs of Groups 4 and 5. Their complexities make them more difficult to achieve during sputter deposition at low temperatures, i.e. when the diffusion rate is limited. They are, therefore, more likely to show a phase evolution similar to that seen for weak carbide formers [9]. These principles have also been applied to binary alloys (i.e. ternary Me-Me-C systems). Both the glass-forming ability [10] and the carbon required for a-C formation [11] can be tuned by varying the ratio between stronger and weaker carbide-forming metals.

The change from a single phase to a TM/a-C nanocomposite typically leads to significant changes in the properties. Crystalline carbides are hard but brittle. Some nanocomposites have, on the other hand, been

* Correspondence to: Department of Chemistry – Ångström laboratory, Box 538, Lagerhyddsvägen 1, SE-75121 Uppsala, Sweden.

E-mail address: leon.zendejas.medina@kemi.uu.se (L. Zendejas Medina).

<https://doi.org/10.1016/j.mtcomm.2023.107389>

Received 21 July 2023; Received in revised form 10 October 2023; Accepted 19 October 2023

Available online 21 October 2023

2352-4928/© 2023 The Author(s). Published by Elsevier Ltd. This is an open access article under the CC BY license (<http://creativecommons.org/licenses/by/4.0/>).

shown to possess a rare combination of high hardness and toughness [5]. The high conductivity of the metal carbide combined with the softness of the a-C phase can also result in a very low contact resistance [6]. Composites with higher a-C content have excellent tribological properties, as carbon can act as a solid lubricant [12]. Furthermore, since carbon is highly inert, the corrosion resistance of TM/a-C coatings can also be high [13,14]. This makes these materials ideal for coating electrical contacts in corrosive environments, for example, the bipolar plates in PEM fuel cells [15].

Recently, there has been an interest in adding carbon to high entropy alloy (HEA) coatings, which are alloys that contain near-equimolar concentrations of many metals [16]. The principles are similar to those for binary alloys. However, since HEAs are mixtures of metals that can have very different carbon affinities, the risk of metal segregation in the material is high. Most studies on HEAs with added carbon have been on HEAs with only strong carbide formers, which can form single-phase high entropy carbides through sputter deposition. Only very few studies exist of HEA/a-C nanocomposites where strong and weak carbide-forming elements were mixed [17,18] and no studies exist yet on nanocomposites based on HEAs with mostly weak carbide formers. The risk in such a system is that the difference in carbon affinity will lead to a separation of the metallic elements and the formation of carbide particles that cause embrittlement and enhance pitting corrosion. These problems were reported when adding carbon to the well-known HEA CoCrFeMnNi through bulk techniques [19,20]. However, magnetron sputter deposition of the same composition should yield very different results. The rapid quenching of atoms from the gas phase to the solid phase has been known to suppress the formation of carbides [21] and create homogenous materials [22]. A related effect was observed when 316 L stainless steel (which has a similar ratio of strong and weak carbide formers as the CoCrFeMnNi HEA) was deposited by sputtering in an acetylene atmosphere [23]. No metal carbides were formed and the metallic elements were found homogeneously distributed in a metallic phase surrounded by a carbon matrix. These composite coatings were reported to exhibit superior mechanical, tribological, and corrosion resistant properties. Similar microstructures may be possible in HEAs.

The aim of this paper is to study the deposition of HEA/a-C nanocomposites based on alloys with different average carbon affinities, and determine the correlation between carbon content, structure, and selected properties. As one model system, we have selected the Cantor alloy, CoCrFeMnNi, which consists of weak carbide-forming metals (Co, Ni, Fe) and metals with a modest carbide-forming ability (Cr, Mn). In addition, we have selected a quaternary alloy CrFeNiTa which contains one very strong carbide-forming metal, Ta. The coatings are magnetron sputtered using graphite as a carbon source to avoid the influence of hydrogen in the carbon phase. They are then analysed with diffraction, electron microscopy, and electron spectroscopy. Thermodynamic modeling using the CALPHAD method is used to interpret the results. Mechanical testing of coatings continues to be a challenging problem in the field of materials science. In this work, several methods will be combined to obtain a clearer picture of the hardness and deformation mechanisms of the coatings, as well as their resistance to cracking at up to 16 % strain. For this purpose, two modes of nanoindentation will be used. Additionally, fragmentation analysis through tensile testing inside a scanning electron microscope will be employed to obtain quantitative information regarding the cracking. Finally, the corrosion resistance will be evaluated with electrochemical tests.

2. Experimental

2.1. Thermodynamic calculations

The phase equilibria in multicomponent materials systems can be predicted using CALPHAD, a method used extensively to describe the thermodynamic properties of alloys [24]. The Gibbs free energy of each phase is first computed. This thermodynamic information can then be

used as input for further calculations, such as equilibrium phase diagrams. In this work, phase fractions and phase compositions for the CoCrFeMnNi(C) and CrFeNiTa(C) systems at equilibrium were determined by CALPHAD calculations using the Thermo-Calc software packages [25] and the CALPHAD thermodynamic database for HEAs, version 3, from Thermo-Calc [26] (TCHEA3). The results were used as guidance when interpreting the experimental data.

2.2. Combinatorial magnetron sputtering

To obtain coatings with different carbon contents, a combinatorial magnetron sputter deposition system with four magnetrons was used. The magnetrons were placed around the substrate holder at a distance of 13 cm and an angle of 16° from the substrate normal. Two or three targets were then used to create coatings with a range of carbon concentrations during the same deposition, thus making it easier to study the trends in phase formation relating to the carbon content. The gradient coatings of the CoCrFeMnNi(C) system were deposited using a graphite target from Kurt J Lesker (99.999 % pure, 76 mm diameter) and an equimolar, spark plasma sintered CoCrFeMnNi target (76 mm diameter) from Plansee Composite Materials, Germany. The gradient samples of the CrFeNiTa(C) system were deposited with the same graphite target, a Ta target from Kurt J Lesker (99.95 % pure, 51 mm diameter), and a spark plasma sintered CrFeNi target (76 mm diameter) from Plansee Composite Materials, Germany. The working gas, Ar, was supplied with a flow of 30 sccm and the working pressure was 0.4 Pa. The target power of the graphite was set to 185 W for both composite alloys, while the powers of the CoCrFeMnNi, CrFeNi, and Ta targets were set to 35 W, 50 W, and 8 W, respectively.

The goal of the deposition was to achieve a large range in carbon content over the gradients and a relatively similar thickness. The large difference in C content was achieved by focusing the CoCrFeMnNi, Ta, and CrFeNi targets on the middle of the substrate holder while tilting the graphite target down and away from the focused position by 26° degrees. The substrate holder was not rotated. This setup resulted in a relatively small variation in the deposition rates for the metals and a large difference in the deposition rate for C over the different positions on the substrate holder. The total deposition rate varied by up to 15 %. This resulted in a thickness difference that was deemed acceptable for the current study. The average deposition rate was found to be around 8 nm/min for the CoCrFeMnNi(C) coatings and around 5 nm/min for the CrFeNiTa(C) coatings. The deposition times were then chosen to achieve approximately 900 nm thick coatings, i.e., 110–180 min. The coatings were deposited on oxidized Si wafers, as well as on strips of polyimide for the mechanical tests. Prior to deposition, all the substrates were cleaned in an ultrasonic bath in acetone for five minutes, followed by the same procedure with ethanol, and then dried with N₂ gas. Before the deposition started, the substrates were cleaned with a – 150 V substrate RF bias. A substrate bias of – 100 V was also applied during the deposition to achieve smoother coatings. No heating was applied, which resulted in a varying substrate temperature during the depositions due to heating from the plasma. The temperatures reached at least 80 °C, which was approximated with a thermocouple attached to the substrate holder (most likely a slight underestimation of the temperature on the substrate surfaces).

2.3. Characterization

The coating morphology was studied with scanning electron microscopy (SEM). Cross-section electron images were recorded in a Zeiss Merlin instrument using the in-lens detector and a field emission gun (FEG) operating at 3–5 kV acceleration voltage. Relative concentrations of constituent metals were recorded with energy-dispersive X-ray spectroscopy (EDS), using an 80 mm² silicon drift detector in a Zeiss 1530 instrument with a voltage of 15 kV. This data was analysed with AZtec (INCA energy) software.

Transmission electron microscope (TEM) analyses were performed at 200 kV with a Titan Themis instrument from Thermofisher (previously FEI), and the EDS was acquired with a SuperX unit from Oxford instruments. The TEM lamellae were prepared in plan-view using a Crossbeam550 instrument from Zeiss. This non-standard preparation required a few modifications of the FIB polishing and was performed based on the procedure proposed by Zeiss. The sample was first coated with protective carbon and a large rectangle of $15 \times 6 \mu\text{m}$ was lifted out at 0° tilt, deep enough to include the whole coating. The raw lamella was then soldered to the TEM grid lying horizontally (0°) and this latter was tilted back to the standard vertical position ($+90^\circ$) before starting the ion milling. The polishing was finely monitored to obtain the center of the coating in the transparent region of the lamella and cleaned using a mild ion beam accelerated at 2 kV for each side. The EDS data was processed using the Hyperspy python package [27].

The time-of-flight elastic recoil detection analysis (ToF-ERDA) measurements were carried out at the Tandem Laboratory at Uppsala University [28,29]. 44 MeV $^{127}\text{I}^{8+}$ ions probed the sample at a grazing angle of 22.5° relative to the sample surface. The ToF-ERDA detector was placed at 45° relative to the forward beam path. The data was analysed using the Potku software. This was used to quantify the lighter elements H, N, C, and Ar.

The chemical environment of carbon was studied using X-ray photoelectron spectroscopy (XPS) in a PHI Quantera II 2000 scanning XPS microscope with monochromatic Al K_α radiation. The analysis area was $100 \mu\text{m}^2$, and the samples were etched using 200 eV Ar^+ ions for 15 min before measuring, to remove the surface oxides and contamination. The C1s peak was deconvoluted through peak fitting in the Igor Pro software. The C-Me component was fitted using a single asymmetric Doniach-Sunjić peak profile. The remaining components had symmetric Voigt peak profiles. A Shirley function was used to fit the background.

The crystalline phase content of the coatings was assessed by X-ray diffraction. θ -2 θ scans were performed with Bragg-Brentano geometry in a Bruker D8 Advance diffractometer with Cu K_α radiation and a Lynxeye XE-T detector. The scans ($2\theta = 20$ – 100°) were performed with a step size of 0.02° and 0.2 s/step. Additionally, GI-XRD measurements were performed in a D8 Discover instrument using a grazing angle of 1° . The primary optics were a Göbel mirror, and a 0.1 mm slit, while the secondary optics were a parallel plate collimator with 0.4° divergence and a Lynx-Eye XE detector used in 0D mode.

2.4. Nanomechanical testing

The hardness and elastic modulus of the coatings were evaluated by nanoindentations with a CSM instrument using a Berkovich diamond tip. Indents were made at a loading rate of 2.5 mN/min down to a depth of 50 nm, which was $< 7\%$ of the coating thickness for all the tested samples (see Table 1). The indentation hardness (H) and reduced Young's modulus (E_r) were calculated using the Oliver-Pharr method [30]. The deformation was also studied qualitatively by nanoindentation using a cube corner diamond tip. Indents were made using

the maximum load of the instrument, which was 50 μN . The cube-corner tip was used, instead of the Berkovich tip, to achieve a higher strain for the same load, thus increasing the probability of crack formation. These indents were studied with SEM imaging in the Zeiss Merlin and Zeiss 1530 instruments described above, using secondary electron detectors and different sample tilts. Both types of indents were made with load control and an acquisition rate of 10 Hz. The Berkovich tip was calibrated with Al_2O_3 .

The crack resistance of the samples was studied with in situ fragmentation tests [31], using a Hitachi scanning electron microscope operating at 15 kV acceleration voltage on a Deben tensile stage. The samples were coatings deposited on $4 \times 10 \text{ mm}^2$ polyimide strips. The crack accumulation was studied in situ while the samples were stretched using a displacement rate of 0.1 mm/min. Fragmentation diagrams were obtained by plotting the crack density, CD, as a function of tensile strain.

The cracking behavior was then modeled. In the crack accumulation process, the density of cracks, CD, as a function of applied tensile strain is represented by the cumulative distribution function

$$F(\sigma) \approx \text{CD}(\sigma) / \text{CD}_\infty = 1 - \exp \left(- \left(\frac{\sigma}{\sigma_\infty} \right)^\rho \right) \quad (1)$$

where CD_∞ is the crack density at saturation, σ is the stress in the coating, and σ_∞ and ρ are the Weibull shape and scale parameters. This method has been applied primarily to brittle coatings, for which the stress in the coating can be determined by Hooke's law $\sigma = \bar{E}\epsilon$, where $\bar{E} = E/(1 + \nu^2)$. However, in a previous work by our group, it was found that the C content in these coatings could change the mechanical behavior to either ductile or brittle [22]. This change strongly affects the cracking process, and, in more ductile coatings, the model based on Hooke's law is not suitable. To account for this brittle-to-ductile transition, the material model was changed by adding a second term to describe the plastic behavior of the coating. The stress is then

$$\sigma = \begin{cases} \bar{E}\epsilon, & \epsilon \leq \epsilon_Y \\ \sigma_Y + \frac{\bar{E}H}{\bar{E} + H}(\epsilon - \epsilon_Y), & \epsilon > \epsilon_Y \end{cases} \quad (2)$$

where σ_Y is the yield stress, H is the hardening modulus and the strain at onset yielding is $\epsilon_Y = \sigma_Y/\bar{E}$. The fracture strain in the coating can be estimated by inserting the Weibull fracture strength σ_∞ in Eq. (2) which yields

$$\epsilon_f = \frac{\sigma_\infty - \sigma_Y}{\frac{\bar{E}H}{\bar{E} + H}} + \epsilon_Y \quad (3)$$

The model is phenomenological and describes the plasticity behavior of the coatings as linear. Here, the main objective is to include the ductile behavior in the fragmentation diagrams and estimate material properties by curve fitting. The two models, with and without accounting for plasticity, are compared in SI Fig. 1 and their goodness of fit is presented in SI Table 1. It is clear that the additional term is required to fit the behavior of the more ductile coatings. Assessing material

Table 1

Approximate atomic concentrations at the positions selected for analysis. C, O, and Ar were quantified using ToF-ERDA while the relative concentrations of Cr, Mn, Fe, Co, Ni, and Ta were measured with EDS in SEM. The sample IDs denote the elements additional to Cr, Fe, and Ni, while LC, MC, and HC are used for low, middle, and high concentrations of carbon. The ordinary thickness values are valid for the samples used for mechanical tests. Some characterization and corrosion tests were performed on samples deposited to a lower thickness on oxidized Si substrates. This value is noted within brackets.

Sample ID	Relative metal content (at%)						Conc. (at%)			Thickness (nm)
	Cr	Mn	Fe	Co	Ni	Ta	C	O	Ar	
Mn/Co LC	20	19	21	20	20	–	25	1	< 1	950
Mn/Co MC	19	22	21	19	19	–	33	1	1	960
Mn/Co HC	19	22	21	19	19	–	49	1	2	900
Ta LC	28	–	28	–	25	19	22	< 1	< 1	900 (640)
Ta MC	25	–	27	–	25	23	33	< 1	< 1	810 (580)
Ta HC	25	–	28	–	27	20	44	1	1	770 (550)

properties in the plastic region of thin coatings is not a trivial task. Here it is shown that these properties can be studied via fragmentation tests using this simple model.

2.5. Electrochemical analysis

The electrochemical experiments were performed using a three-electrode electrochemical cell connected to an Autolab potentiostat. A 0.05 M H_2SO_4 aqueous solution served as the electrolyte and the samples were used as working electrodes. The reference electrode was an Ag/AgCl (3 M NaCl) reference electrode (RE), while a Pt wire functioned as the counter electrode (CE). All measurements were performed at room temperature. First, the samples were kept in the electrolyte solution for 45 min under open circuit potential (OCP) conditions. Next, three consecutive polarization curves were recorded. The first time, the potential was swept from -0.7 to $+0.7$ V vs. Ag/AgCl, while the second and third scans started at 0 V and ended at $+0.7$ V vs. Ag/AgCl. Between the scans and at the end of the experiment, the OCP was recorded for five minutes.

3. Results and discussion

3.1. Phase formation predictions through thermodynamic calculations

Thermodynamic calculations with the CALPHAD method were used to predict the phase constitution of the synthesized samples. The metal compositions used for the calculations were $\text{Co}_{20}\text{Cr}_{20}\text{Fe}_{20}\text{Mn}_{20}\text{Ni}_{20}$ and $\text{Cr}_{26}\text{Fe}_{27}\text{Ni}_{27}\text{Ta}_{20}$, which are close to the concentrations obtained with EDS (see Table 1). The results are shown in Fig. 1(a) and (b), which display the phase fractions at equilibrium at 500°C and for carbon concentrations from 0 to 50 at%. Since the synthesis with magnetron sputtering takes place close to room temperature, a low temperature was chosen for the calculations. However, at low temperatures, there are less thermodynamic data available. 500°C was therefore considered to be the lowest temperature for which reliable predictions could be obtained. To make the graphs clearer, all the alloy phases (solid solutions and intermetallics) and all the Cr-rich carbides were grouped together and only the sums of their fractions are displayed. The alloy phases included fcc, bcc, and a σ phase in both materials systems, and C14 Laves and Ni_3Ta phases in the CrFeNiTa(C) system. The Cr-rich carbides included M_{23}C_6 , M_7C_3 , and M_3C_2 , which contained a smaller amount of the remaining elements. The fraction of the Ta-rich carbide, TaC, is displayed separately.

Both systems were predicted to segregate into multiple phases at all temperatures and all carbon concentrations within the chosen range. At 500°C , there was no solubility of carbon in the alloy phases, so any addition of carbon is expected to result in the formation of metal carbide phases. The graphite phase, which is of particular interest for this study, was formed above a certain carbon content which was different in the two materials systems. The minimum concentration of C for graphite formation was 25 at% in the CoCrFeMnNi system and 33 at% in the CrFeNiTa system. This difference is expected since the CrFeNiTa alloy has a higher average carbon affinity.

To assess the validity of the thermodynamic calculations, the amount and quality of available data are key factors. The TCHEA3 database [26], which was used for these calculations, includes a full assessment of all the possible binary subsystems in the two material systems. For the CoCrFeMnNi system, eleven out of the twenty ternary subsystems have been fully assessed, including six metal-carbon ternaries. The remaining systems have only been tentatively assessed. For the CrFeNiTa system, the fraction of fully assessed ternaries is slightly lower, four out of the ten possible systems have been fully assessed, while the remaining have been tentatively assessed. Furthermore, the CALPHAD calculations of the CoCrFeMnNi have been validated through experiments with good agreement; multiple times for the alloy [32], and at least once with added carbon [22]. The CrFeNiTa system has, to our knowledge, not been systematically studied as a bulk material, with or without carbon.

Based on these results, some predictions can be made regarding the synthesis of these materials. It is clear that, if synthesized through traditional bulk methods at high temperatures, they would not possess the desired properties. Several embrittling carbide phases would be formed. The fcc and bcc alloy phases would be depleted of Cr and Ta, which are the two elements that can form a passive layer to slow down corrosion [33]. This means that parts of the material would be left unprotected and selective etching would occur. Even if full segregation could be avoided, the formation of precipitates would increase the risk of pitting corrosion, as in stainless steel [34]. This was observed for CoCrFeMnNi when carbon was added beyond the solubility limit [19].

However, in this work, the aim is to design a metastable coating material by intentionally suppressing the formation of the equilibrium phases. To successfully form a nanocomposite material like the one reported in Ref. [23], the separation of metals into multiple alloy and carbide phases must be suppressed, while the carbon must be allowed to segregate.

Based on the CALPHAD results, the suppression of the separation of metals could be easier in CoCrFeMnNi, since Ta forms binary

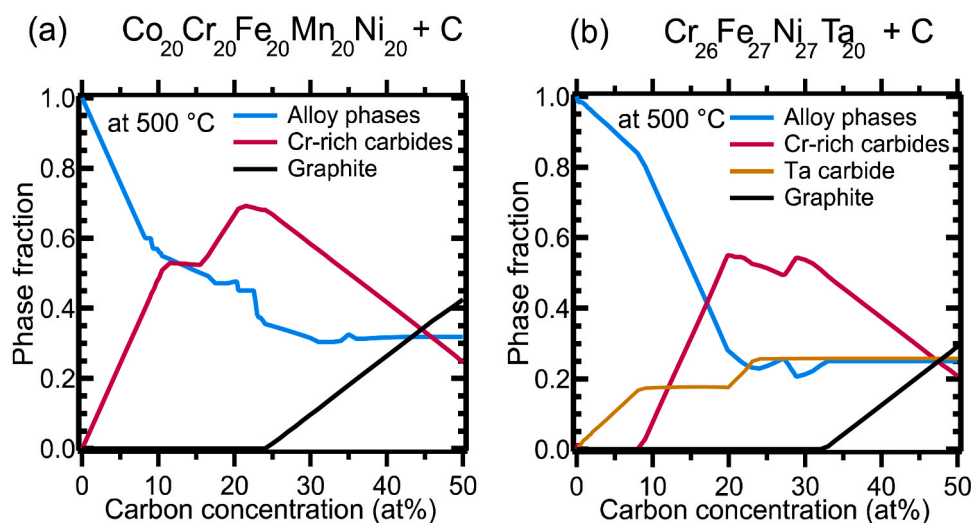


Fig. 1. Phases at equilibrium calculated using the CALPHAD method of the alloys (a) $\text{Co}_{20}\text{Cr}_{20}\text{Fe}_{20}\text{Mn}_{20}\text{Ni}_{20}$ and (b) $\text{Cr}_{26}\text{Fe}_{27}\text{Ni}_{27}\text{Ta}_{20}$ with a varying C content, displayed for carbon contents between 0 and 50 at% and at 500°C .

intermetallic phases with Fe and Ni that have very large negative formation enthalpies [35], including the Ni_3Ta phase. This increases the driving force to segregate. The highly stable Ta carbide with its simple unit cell should also be easier to form than the more complex Cr-rich carbides in the CoCrFeMnNi(C) system. The CALPHAD results also indicate that a free carbon phase forms at lower carbon contents in CoCrFeMnNi . Based on these results, the desired composite materials should be easier to achieve in the CoCrFeMnNi(C) system.

3.2. Composition, structure, and morphology

The first characterization to be performed was measurements of the C1s core levels with XPS. The analysis was performed along a line on the wafer where the carbon content varied while the ratio between the metallic elements was nearly unchanged. The results are displayed in Fig. 2. The target powers for each gradient were chosen so that C1s had only one contributing peak on one side of the wafer, but multiple contributions on the other side. As explained below, the first peak is attributed to carbidic carbon (C in a metal-rich environment), whereas the additional peaks are attributed to free carbon (C in a C-rich environment). The samples are thus compositional gradients that represent the range in carbon content where the free carbon first appears. All the coatings were found to be amorphous in XRD (SI Fig. 2), which will be confirmed later using diffraction in TEM. This indicates that the crystallization was suppressed for all the equilibrium phases. It also shows that the free carbon component observed with XPS is amorphous carbon.

The gradient based on the CoCrFeMnNi alloys will henceforth be named the Mn/Co series, while the gradient based on the CrFeNiTa alloy

will be named the Ta series. Three positions on each of the gradients were selected for in-depth analysis, named low carbon (LC), high carbon (HC), and medium carbon (MC). HC was the position closest and furthest away from the graphite target, respectively. MC was chosen from the middle of the gradient, close to where the free carbon signal was first emerging in the XPS spectra. A full quantification of the composition was only performed on these spots (six in total). Two techniques were combined: EDS to calculate the relative metal concentrations and ToF-ERDA to measure the contents of the lighter elements H, C, O, and Ar. ToF-ERDA could not be used to quantify the metals due to the peak overlaps of heavier elements. The full quantification is found in Table 1. Despite the use of equimolar targets of CrFeNi and CoCrFeMnNi , the composition of these metals varied slightly over the surface of the gradient. The carbon content was found to be between 25 and 49 at% for the Mn/Co series and between 22 and 44 at% for the Ta series. The oxygen contamination was 1 at% or lower for all the samples. A signal from Ar was also detected, and this was higher for the HC samples. The Ar was most likely incorporated during the deposition process, and this was enhanced by the use of a substrate bias which increases the energy of the Ar^+ ions in the plasma, thus allowing them to penetrate deeper into the material. No H was detected in the coatings.

The C1s peaks in Fig. 2 were deconvoluted to quantify the contributions from metallic and free carbon, respectively. An example of the fitted peaks of the HC samples is displayed in Fig. 2(a) and (b). The C-C component was found to consist of two contributing peaks, which had binding energies in the range for carbon in sp^2 (284.1 eV) and sp^3 (285.0 eV), respectively [36]. A weak contribution was also found at higher binding energies (286.4 eV), which was attributed to carbon in a

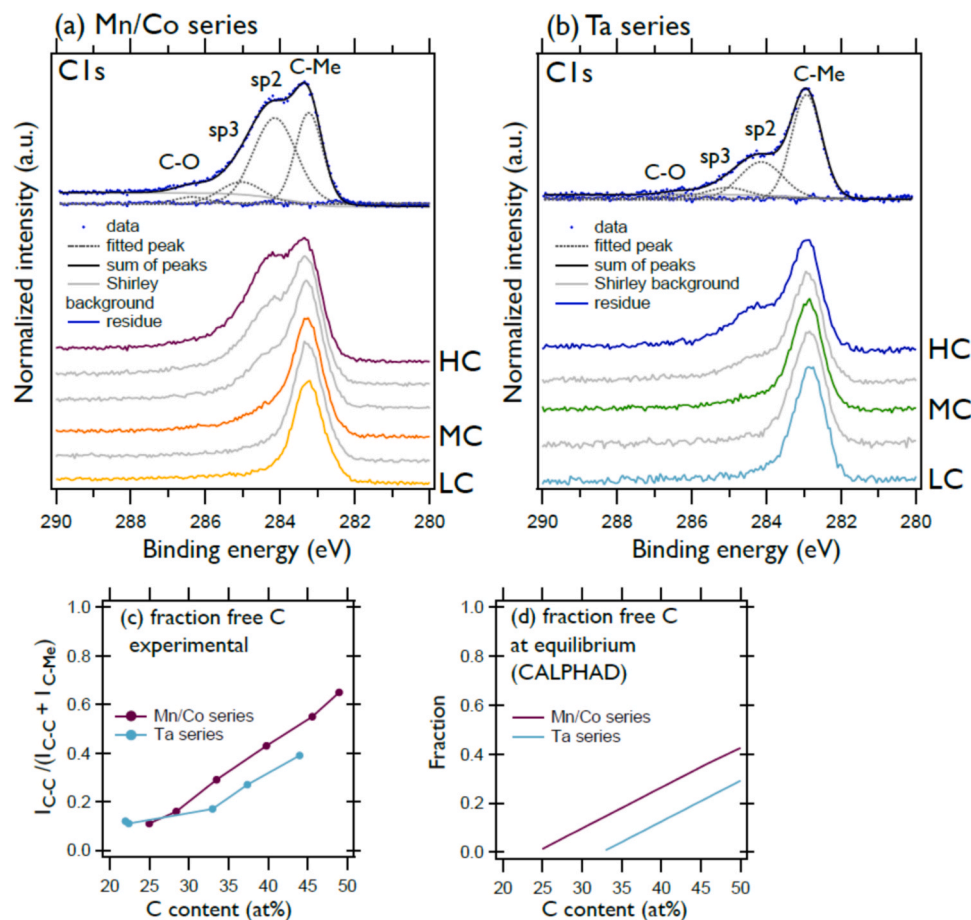


Fig. 2. C1s core level spectra measured at different points on the combinatorial samples of (a) the Mn/Co system and (b) the Ta system including an example of the peak fitting of this region. (c) shows the experimentally determined fraction of carbon in a C-C environment while (d) displays the fraction of carbon found in the graphite phase calculated with the CALPHAD model at 500 °C for different carbon contents.

C-O environment due to the small O contamination [37]. The sp^3 component was around 20 % of the total C-C contribution, similar to values reported for amorphous magnetron sputtered a-C coatings [38, 39]. A supplementary Raman analysis was performed on the two HC samples, which confirmed that there was amorphous carbon with predominantly sp^2 bonding (SI Fig. 3).

From the fitted peak areas, the total fraction of carbon in a C-C environment (sp^2 and sp^3) was calculated. The area of the C-O peak was excluded from this calculation. The results, presented in Fig. 2(c), show that the amount of free carbon increased linearly with the carbon content. The slope was close to unity in the linear part of the curves. This indicates that, once graphite started to form, all the additional carbon was incorporated into the free carbon phase. For the same carbon concentration, there was more free carbon in the Mn/Co series than in the Ta series. This coincides with the prediction from CALPHAD, which showed that the formation of a graphite phase required a higher carbon content in the CrFeNiTa system. At the lowest carbon contents, the calculated fraction of carbon was 0.1 for both sample series. In Ref. [23] the fraction of C-C in 316 L stainless steel with added carbon was calculated from XPS data and it was found that the value plateaued below 30 at% carbon at a value of around 0.1. It was also found that, below this concentration, the materials did not display the typical properties of the carbon composite. This indicates that the small fraction of C-C found at low carbon concentrations was not due to the formation of a free carbon phase. It could rather be related to contamination from the ambient atmosphere that cannot be fully removed by the Ar^+ etching.

To further explore the connection between the deposited samples and the predicted equilibrium phases, the fraction of carbon found in graphite at 500 °C was extracted from the calculated equilibria in Section 3.1 and presented in Fig. 2(d). The curves look similar to the experimentally determined fractions in Fig. 2(c). The fraction increases linearly with added carbon and is consistently higher for the Mn/Co alloy system. If the assumption is made that some of the C-C signal comes from contamination and the experimental curves are shifted down by 0.1, they overlap with the calculated curves. This shows how thermodynamic calculation can be useful for understanding and predicting the phase formation in amorphous coatings, even though they are non-equilibrium materials.

The peak fitting also revealed chemical shifts in the C-Me peak. For the CoCrFeMnNi series, the C-Me peak was found at the same binding energy, 283.23 eV, regardless of the carbon content. In the Ta series, the binding energy was around 282.9 eV for all the samples. C1s in TaC is reported to have a slightly lower binding energy than Cr_7C_3 and carbides with Fe and Mn [40,41], although the literature values feature a broad range, as explained in ref [40]. The shift could therefore be explained by the added Ta in the C-Me environment.

The SEM micrographs in Fig. 3 show the tilted cross-sections of the samples. For both series, the surface of the LC composition was completely smooth and featureless. The fracture surface, however, displayed a vein pattern. This is typically formed from the movement of shear bands, which is a deformation mechanism in amorphous materials [42] and is not a sign of pre-existing structures in the material. For the MC and HC samples, the surfaces of the coatings were not smooth but displayed some granular features. In their fracture surfaces, no vein patterns were seen. The Ta MC sample displayed, instead, a faint granular pattern. The remaining samples had a clearly granular microstructure which also appeared to be columnar for the Ta HC sample. The more granular morphology can be explained by the formation of a two-phase material when free carbon begins to form.

All the coatings had small nodular defects, which were most likely created due to flakes from the targets contaminating the surface in the sputter-down geometry of the deposition chamber. There were around 100 defects/ mm^2 and they varied in size from 10 nm to several micrometers in diameter. They were not more prevalent in any of the compositions. These defects will be revisited in Section 3.3.2., where the

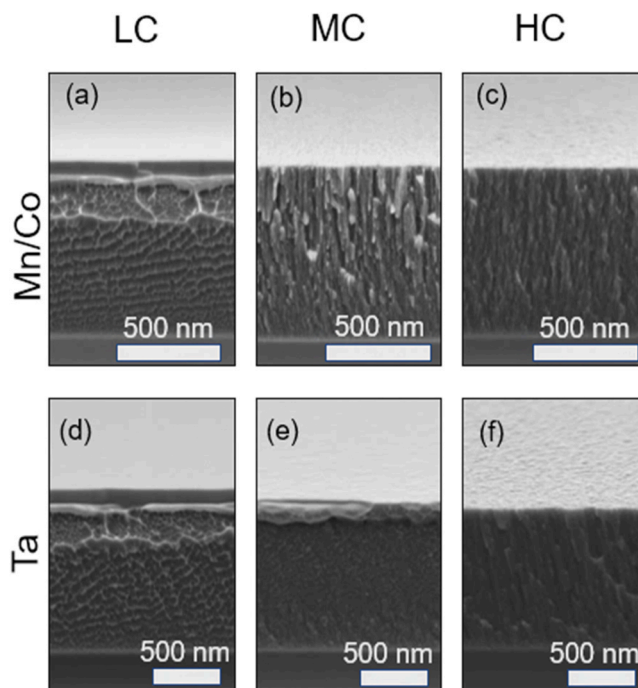


Fig. 3. Tilted SEM cross-section micrographs of the coatings used in the study, recorded with the in-lens detector by tilting the fracture surfaces 10° relative to the electron beam.

crack resistance of the coatings is analysed.

TEM studies were performed on plane-view lamella of three selected samples, Mn/Co HC, Ta HC, and Ta MC. The purpose was to observe the distribution of free carbon in the HC samples. Ta MC was included to study the materials with very low fractions of free carbon. With SAED, it was confirmed that the samples were amorphous since no spots or sharp rings could be seen, only diffuse halos. The STEM image of the Ta MC coating in Fig. 4(a) showed no fine structure, it had the appearance of a single-phase material. The EDS analysis showed a random distribution of the elements without any indication of segregation. In contrast, the Ta HC coating exhibited a two-phase microstructure with darker grains surrounded by a thin and web-like matrix phase (Fig. 4b). This picture agrees with the XPS analysis in Fig. 2(b). The EDS analysis confirmed that the light region is the carbon-rich amorphous phase detected with XPS. The a-C phase was clearly depleted in Fe, Cr, and Ni, while the Ta was more evenly distributed. The STEM image for the Mn/Co HC coating in Fig. 4(c) shows a significant amount of the lighter carbon-rich phase surrounding the darker metal-rich grains. The thickness of the a-C phase was larger than in the Ta HC sample and the size of the metal-rich grains was smaller. The EDS confirms a high carbon content in the matrix phase and an enrichment of Cr, Co, Fe, and Ni in the grains. The Mn was more evenly distributed between both phases (Fig. 4f).

Comparing the present results to those for the 316 L/a-C coatings studied in Ref. [23], there are some clear differences. In both cases, the phase composition changed from single-phase amorphous coatings to amorphous nanocomposite coatings with increased carbon content. However, the microstructure in the 316 L/a-C coating in Ref. [23] was organized into long, cylindrical grains of the metallic phase with uniform size and an even layer of a-C between them. The TEM studies in the present study showed a much more randomly organized material, with a larger distribution of grain sizes and varying thickness of the a-C phase. The lack of such a structure in the present study could be due to the lower deposition temperature limiting the diffusion rate or the fact that a graphite target was used as the carbon source instead of acetylene.

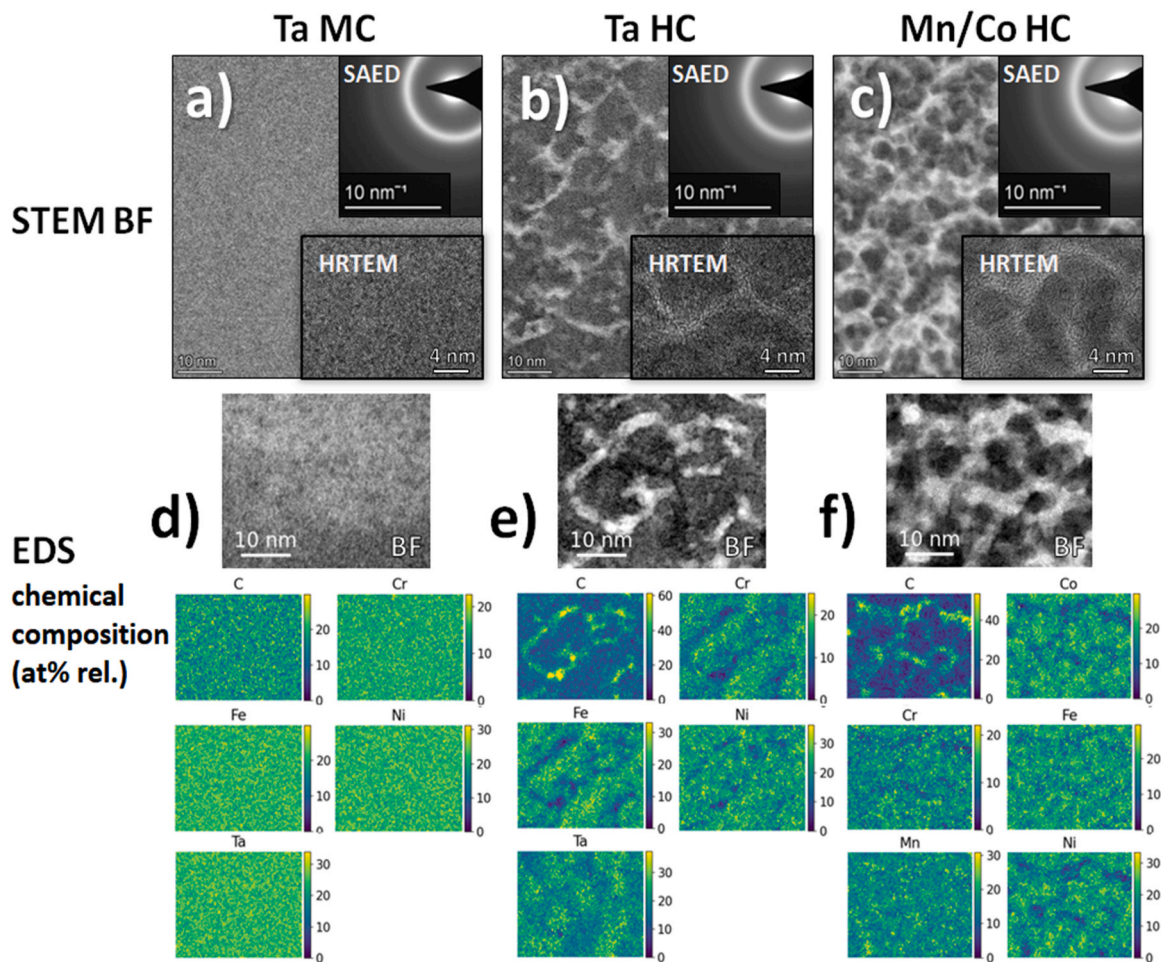


Fig. 4. TEM studies of three selected compositions: Ta MC, Ta HC, and Mn/Co HC including STEM and HRTEM micrographs, SAED patterns displaying the diffuse rings, and EDS maps showing the elemental distribution.

3.3. Mechanical properties

3.3.1. Hardness, elastic modulus, and local deformation

The mechanical properties of the samples were assessed using multiple methods. First, nanoindentation was performed with a Berkovich tip. The Oliver-Pharr method was used to calculate the indentation hardness and the elastic modulus of the coatings, presented in Table 2. For both sample series, the hardness and the elastic modulus were higher for the LC samples. The hardness of Ta LC (13.3 GPa) was also significantly higher than for Mn/Co LC (11.5 GPa), while the elastic modulus was not significantly different. The lower hardness for increasing carbon content can be attributed to the presence of the a-C phase, which is softer. For the Ta series, the LC and MC samples had the same hardness and elastic modulus, while the Mn/Co had a significantly lower hardness

at MC. This is most easily explained by the fact that the free carbon contribution was lower at the Ta MC position, only 5 % higher than the baseline C-C fraction (0.1), compared to 18 % higher for the Mn/Co MC.

The mechanical properties of nanocomposites depend, among other factors, on the volume fractions and shapes of different phases. The elastic modulus of a composite can be modeled using the Halpin-Tsai equation [43]:

$$E_c = E_m(1 + 2sqV_p)/(1 - qV_p) \quad (4)$$

where $q = (E_p/E_m - 1)/(E_p/E_m + 2s)$, E_p and E_m are the elastic moduli of the particles and the matrix, respectively, V_p is the volume fraction of the particles and s is the aspect ratio of the particles. This entails that, if the moduli of each phase are known, the volume fractions can be estimated. Here, we will estimate the volume fraction of carbon in the two HC

Table 2

Summary of properties of the samples calculated using data from different techniques. The fraction of carbon in the a-C phase was calculated from XPS results, the indentation hardness (HIT) and reduced Young's modulus (E_r) from nanoindentation, and the yield stress (σ_y), hardness modulus (H), fracture strain (ϵ_f), Weibull scale parameter (σ_∞), and Weibull shape parameter (ρ) were calculated from fragmentation test data.

Sample ID	XPS	Nanoindentation		Fragmentation tests				
	Free carbon fraction	HIT (GPa)	E_r (GPa)	σ_y (GPa)	H (GPa)	ϵ_f (%)	σ_∞ (GPa)	ρ (dimensionless)
Mn/Co LC	0.11	11.5 ± 0.2	171 ± 2	2.4	38	5.5	3.0	2.0
Mn/Co MC	0.29	10.4 ± 0.2	168 ± 4	1.5	30	4.3	2.8	1.7
Mn/Co HC	0.65	8.7 ± 0.2	136 ± 2	1.3	20	4.2	2.1	2.4
Ta LC	0.12	13.3 ± 0.2	170 ± 2	4.3	53	4.3	4.0	1.8
Ta MC	0.17	13.2 ± 0.2	171 ± 2	2.5	53	3.7	3.3	1.5
Ta HC	0.39	11.5 ± 0.2	139 ± 2	1.6	53	3.8	3.2	1.5

samples using some key assumptions and compare the results to the fractions extracted from STEM images (Fig. 4). The purpose is to investigate the deviation between the two methods, which will most likely be due to a faulty assumption about the grain shape (i.e. aspect ratio).

The elastic modulus E_p was assumed to be the modulus for the LC sample. The mechanical properties of magnetron sputtered amorphous carbon depends strongly on the fraction between sp^2 and sp^3 bonds [44]. Therefore, the elastic modulus of the surrounding a-C matrix, E_m , was taken as the literature value (80 GPa) for a magnetron sputtered coating with a similar sp^2/sp^3 ratio [39]. The aspect ratio was assumed to be unity since the shape of the grains was unknown. The carbon volume fractions for Mn/Co HC and Ta HC were thus calculated to 31 % and 28 %, respectively.

The volume fractions were then estimated from STEM (Fig. 4) using the area fractions of each phase. The estimated values were around 30 % for Mn/Co and 16 % for Ta HC. The value for Mn/Co was more difficult to extract, and, therefore, less certain. This was because the contrast difference between the metallic phase and the a-C phase was not as clear. This indicates that multiple grains of the metallic and a-C phase were superimposed in the lamella, which points to a less columnar morphology with more rounded grains. This is supported by the cross-section SEM images in Fig. 3; the morphology is more clearly columnar for the Ta HC coating and less so for Mn/Co HC.

From this analysis, we can conclude that the two methods for estimating the volume fraction yielded more similar results for the Mn/Co HC sample, and that the value appears to be overestimated using the Halpin-Tsai equation for the Ta HC sample. Considering the more columnar morphology of this sample, the larger discrepancy is easiest explained by the aspect ratio. Another source of error for both samples is faulty assumptions on the elastic moduli. This includes size effects, since there may be a difference between the moduli of micron scale coatings and the nanoscale particles in the samples.

Fig. 5 shows SEM images of the indents obtained with a cube-corner tip pressed to the maximum load of the instrument, 50 μ N, reaching depths close to the thickness of the coatings. The indents of both LC samples display the typical morphology of amorphous alloys. They

cannot deform through slip planes since they lack long-range order, so they deform in a discontinuous manner through the activation of shear bands [42]. No cracks were visible, but the indents were surrounded by pileups with jagged edges, typically associated with the formation of shear bands. In a previous publication, indents were made on samples with only 6 at% carbon and they displayed the same morphology as seen for the Co/Mn LC sample [22], indicating that the amorphous coating with much less carbon deformed through the same mechanism. The bands were slightly different in the two materials. On the Ta LC sample, the pileup consisted of a few shallow and rounded bands. On the Co/Mn LC sample, there was a larger number of bands, and they were jagged and appeared to be more raised from the surface of the coating. The MC sample had a fine-grained two-phase structure, as seen in SEM and TEM. However, the morphologies of the indents showed evidence of the same uneven deformation that is associated with shear bands. This indicates that it is still deformed similar to a single-phase amorphous alloy. Co/Mn MC was the only sample where radial cracks were observed around the indents, which is evidence of a lower crack resistance. Finally, the indents on the two HC samples were similar to each other and had very different morphologies for the MC and LC samples. They were crack-free and almost completely free from pileups. The smaller pileups indicate a decreased resistance to plastic deformation.

3.3.2. Fragmentation analysis: fractography, fragmentation diagrams, and mechanical properties

The cube corner nanoindentation provided qualitative information on the deformation mechanisms of the different coatings. However, since the strains were not enough to induce cracking in these relatively ductile materials, a comparison of the crack resistance could not be made. To obtain more quantitative information, fragmentation tests were performed. Fig. 6(a) to (f) show representative micrographs of the coatings at two strains during the tensile testing; 1 % and 16 % (shortly before substrate failure). The LC samples formed fewer but broader cracks, while the HC samples formed many thin cracks. For the Ta LC coatings, buckling was also observed at high strains. The cracks were, in most cases, associated with a defect in the coatings. Some cracks were formed at nodular defects, which are a type of imperfection caused by

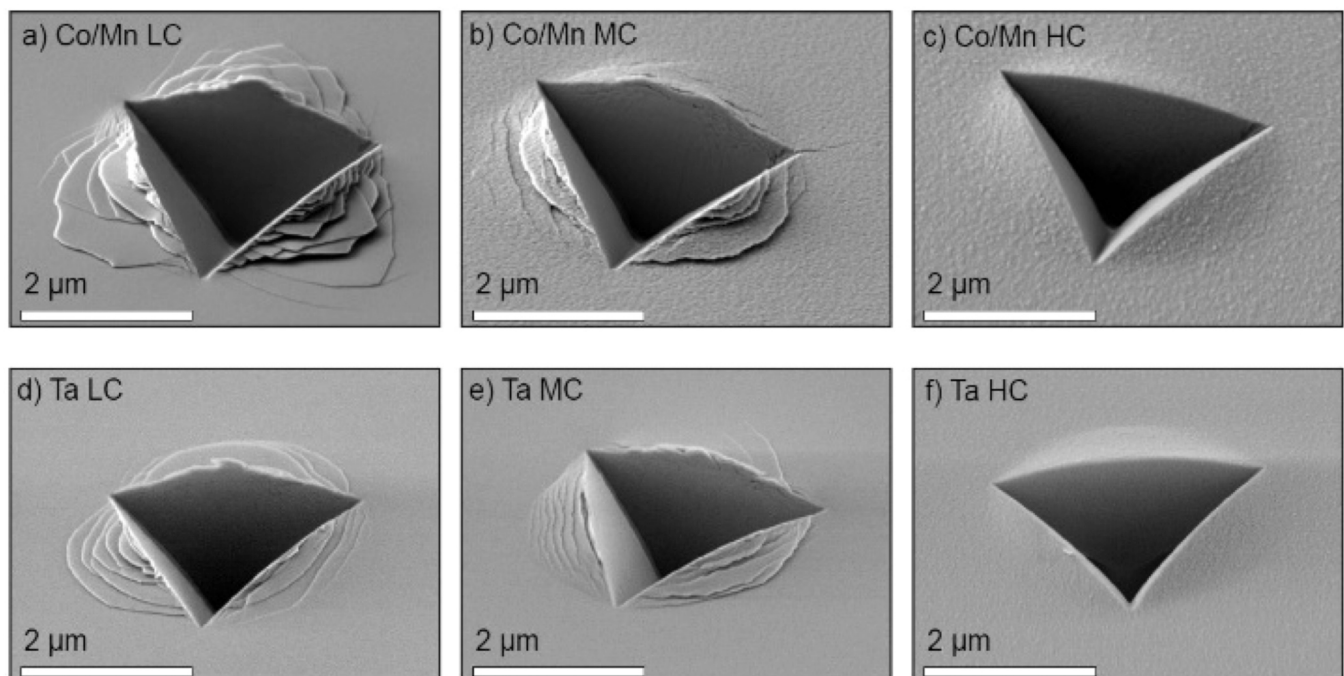


Fig. 5. Micrographs recorded with a secondary electron detector on indents performed with a cube corner tip to a load of 50 μ N. Recorded by tilting the sample surface normal 59° relative to the electron beam.

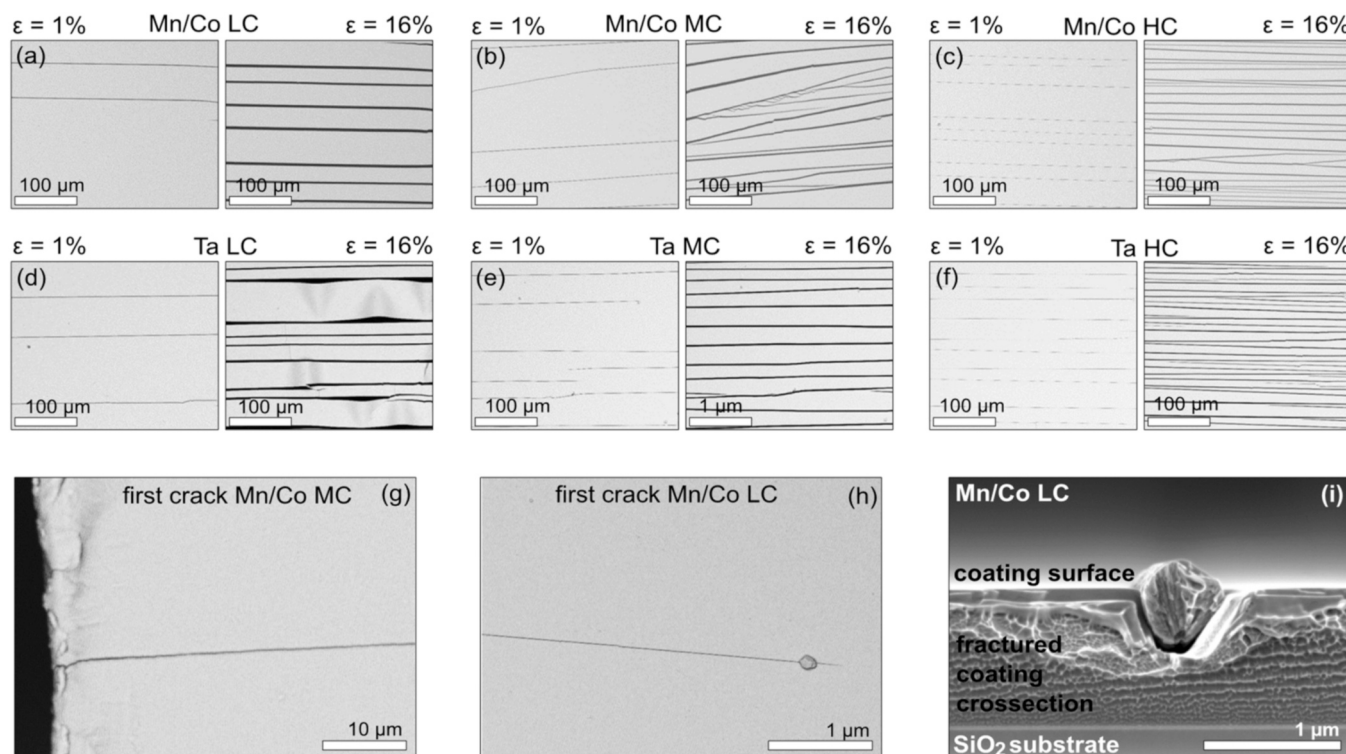


Fig. 6. SEM micrographs of the samples (a) – (f) display the top view images of the samples on polyimide substrates, during the tensile tests at two different strains. (g) and (h) display the first crack formed on two of the samples, to exemplify how the cracks emanate from defects, either from the deposition (nodular defects) or from imperfections in the substrate, which were most prominent on the cut edge of the polyimide strip. (i) is a tilted cross-section image of one coating where a nodular defect could be seen in cross-section.

particles contaminating the surface during the deposition. An example of such a defect is seen in Fig. 6(h) and (i). Other defects were formed at small imperfections in the substrate. Many of the cracks emerged from the edges of the polyimide substrate, which was rough and slightly uneven, leading to the formation of an uneven coating as shown in Fig. 6(g). At higher strains, the MC and HC coatings also formed cracks that were not associated with defects. These were instead branching out from pre-existing cracks. Cracks are expected to initiate at the weakest point in a material, and this observation does not mean that the crack density is necessarily determined by the defect density. As mentioned in Section 3.2, no differences were found regarding the density of nodular defects on the surfaces of the different samples. It appears that the inherent

mechanical properties of the coatings are more important and that even the weakest points are stronger in the LC coatings than in the HC coatings.

Fig. 7 shows the crack density as a function of the tensile strain for the six sample compositions. The crack density increased with the carbon content. In the Ta series, the MC and HC positions had very different crack densities, while Mn/Co MC and Mn/Co HC behaved more similarly. The shapes of the curves were different for the samples with and without free carbon. The LC samples, which had no free carbon, reached crack saturation at around 5 % strain. After this point, no more cracks were formed, but the existing cracks opened wider to accommodate the strain. The remaining coatings did not reach crack saturation during the

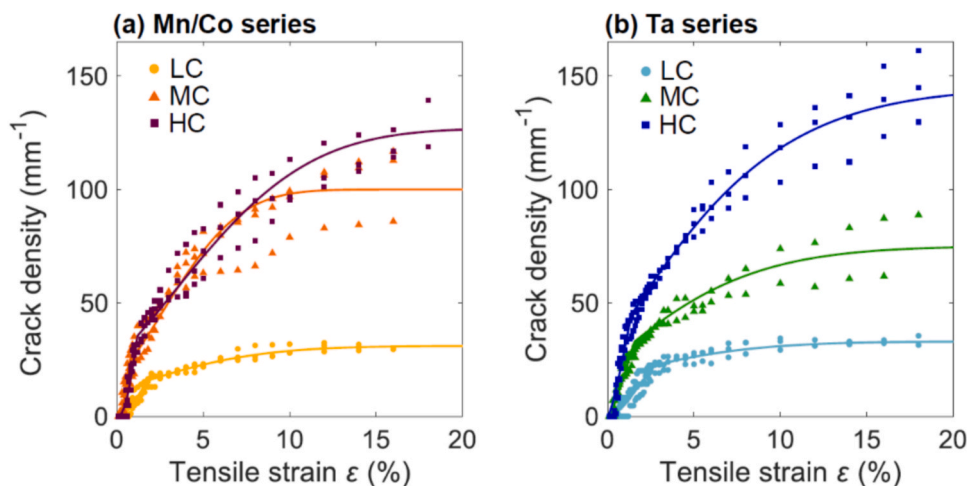


Fig. 7. Fragmentation diagrams displaying the crack density as a function of the tensile strain. The three colours represent the three C-contents. The markers are the experimental data from three fragmentations tests, averaged over three spots on the surface of each sample. The solid lines are the fitted elastic/plastic models.

experiment.

Fitting of the fragmentation data was performed using the equations described in the method section. In a previous publication, where only the amorphous regime was considered, the data could be fitted satisfactorily using only a linear elastic model based on Hooke's law. However, in the present case, this model did not fit the fragmentation data of the MC and HC samples. It was hypothesized that these softer and more ductile coatings go through plastic deformation during the tensile tests. When the plastic deformation was considered in the model, the data could be fitted satisfactorily. A comparison between the two models, with respective R^2 values can be found in the supporting information (SI Fig. 1 and SI Table 1). It showed that the linear elastic model was a satisfactory fit only for the hardest coating Ta LC, while the elastic/plastic model fitted the data of all samples with an R^2 of at least 0.87.

Through the fitting of Eq. (1), the strength of the coating, σ_y could be extracted. Similarly to the indentation hardness, the highest strength was found for Ta LC. However, the Ta MC samples, which were found to have almost the same hardness as the Ta LC samples, had a lower strength in the tensile tests. This indicates that the resistance to deformation depends strongly on the mode of stress. Both the strength and the estimated Weibull fracture strain, ε_f , decreased with carbon addition for both sample series.

It can be concluded from the analysis above that the increase in both hardness and toughness that was reported for the CrFeNi/a-C:H coatings in ref [23] could not be seen for the present samples. This could be because the unique mechanical properties of the CrFeNi/a-C:H coatings were due to the organized nanotubular structure. In the present study, the nanocomposite was not organized in the same manner. The lack of order may be due to the lower deposition temperature, which leads to a limited diffusion rate. It could therefore be possible to achieve similar results as for the CrFeNi/a-C:H coatings by tuning the deposition parameters. However, there are applications where a softer material is preferable, for example, to decrease the contact resistance under load.

It is clear that the single-phase materials had a higher resistance to the formation of cracks than the composite coatings. Again, this does not mean that they would be preferable in an application with large tensile strains. The resistance to cracks led to an early crack saturation, and at high strains, this resulted in an increased widening of the cracks and buckling, which led to delamination. The stronger single-phase coatings may be more beneficial at low strains, where the number of cracks can be limited, while the softer materials may be more beneficial at higher strains where they can continue to form microcracks that dissipate the stress on the coating. To answer this question, tests would be required that are more similar to the intended application.

3.4. Corrosion testing

The corrosion tests were performed in 0.05 M H_2SO_4 . After 45 min under open circuit potential (OCP) conditions, the samples were polarized with linear sweep voltammetry (LSV) from -0.7 to 0.7 V vs. Ag/

AgCl (3 M NaCl). The polarisation was then performed another two times in a shorter potential range: from 0 to 0.7 V. The upper and lower limits of the LSV experiments were chosen to approximate the conditions at the cathode and anode of the bipolar plate in a PEM fuel cell [45]. Between each scan and at the end of the experiment, the cell was kept at the OCP for five minutes to move closer to the steady state of the system. The corrosion tests were performed on the LC and HC samples of both sample series.

The curves from the three repeated scans on the Mn/Co series and the Ta series are displayed in Fig. 8(a) and (b), respectively. For all the samples, the curves for the second and third scans were overlapping and had a higher E_{corr} , lower j_{corr} , and lower currents in the passive region compared to the first scan. This can be explained by the formation of a stable passive layer during the first scan. In the first scan, the LC samples had a lower E_{corr} than the HC samples. In the second and third scans, the curves for Mn/Co LC and HC overlapped. The curves for Ta LC and HC did not overlap, but they moved closer to each other.

To understand the effect of carbon addition, it is necessary to understand its role during corrosion. In a previous study by our group, amorphous CoCrFeMnNi samples with 0, 6 and 11 at% carbon were studied, and the carbon was found to improve the corrosion resistance. Through surface characterization, it was concluded that the carbon was not present at the surface of the samples when they were passivated. The presence of carbon, however, appeared to give rise to a change in the bulk material that suppressed the oxidation reactions [46]. This should also be true for the Mn/Co LC sample in the present study. However, the presence of segregated carbon, as in the HC samples, means that there must be carbon in direct contact with the electrolyte. The corrosion of graphite has been studied previously in acidic environments. The oxidation of carbon to form CO_2 is thermodynamically favorable above 0 V (vs. Ag/AgCl) [33], but this reaction occurs only at high overpotentials. During the corrosion of graphite, oxidized surface groups can form on carbon above 0.3 V [47]. This can be regarded as a kind of passivation since it suppresses further oxidation of the carbon at the surface. In a study by Höglström et al. [14], Cr-C coatings with different contents were studied using LSV measurements. The samples with higher carbon contents had free carbon and they displayed increasing E_{corr} values for higher carbon contents. However, they also had higher currents in the passive region. The authors proposed that the currents were not a sign of breakdown, since the carbon surface was being passivated with oxygen-containing groups. In the present study, this effect was not observed. The currents in the HC samples were found to be similar to or lower than those for the LC samples already after the first scan.

4. Conclusions

Combinatorial sputtering was used to prepare coatings in the CoCrFeMnNiC and CrFeNiTaC systems with a gradient in the carbon content over the surface. Selected positions on the gradient were characterized

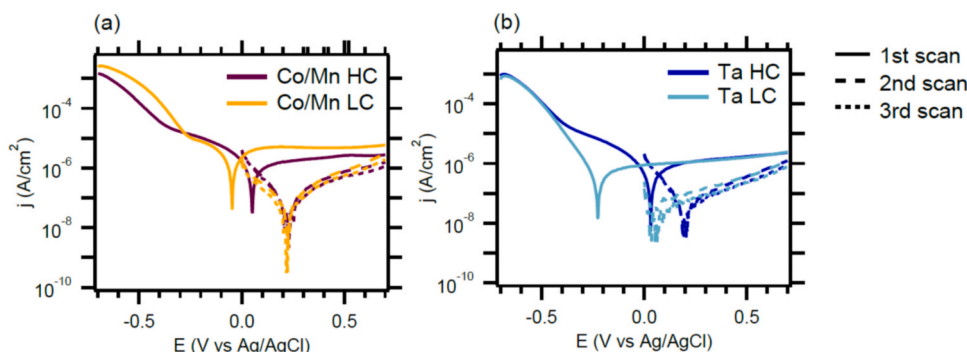


Fig. 8. Polarization curves from three repeated potentiodynamic polarization scans of the samples in 0.05 H_2SO_4 using a scan rate of 1 mV/s.

and assessed with regard to the mechanical properties and corrosion resistance. The main conclusions are:

- CALPHAD calculations predicted the formation of a phase mixture with alloys and carbide phases. Graphite was predicted to form from around 25 at% C in CoCrFeMnNi and around 33 at% C in CrFeNiTa.
- Through magnetron sputtering, amorphous materials were formed, and free carbon (sp^2 and sp^3 -bonded) was observed for carbon contents close to the predicted minimum concentrations for graphite formation. The crystallization and formation of multiple metallic and carbide phases were suppressed for both material systems.
- The mechanical properties of the materials were highly dependent on the amount of free carbon. The hardest coating in the study was the CrFeNiTa alloy with 22 at% C. The samples with high amounts of free carbon were both considerably softer and were similar regarding both hardness and elastic modulus for the two alloy systems.
- Coating fragmentation in tensile tests was used to quantify the crack resistance. The coatings with no free carbon were stronger and formed a lower number of cracks during the tests. After around 5 % strain, the crack density reached a plateau, and the existing cracks became wider. The samples with high amounts of free carbon did not reach crack saturation but continued to form cracks throughout the whole experiment, up to a strain of 16 %. The cracks in these samples were thinner and more closely spaced, and the delamination was less severe.
- The corrosion resistance was generally higher for the samples with free carbon than for the samples with a single amorphous phase. The sample with the highest corrosion resistance was CrFeNiTa with 44 at% C.

CRediT authorship contribution statements

León Zendejas Medina: Conceptualization, Investigation, Formal analysis, Writing – original draft. **Marcus Vinícius Tavares de Costa:** Conceptualization, Methodology, Formal analysis, Writing – original draft. **Olivier Donzel-Gargand:** Investigation, Formal analysis, Writing – review & editing. **Leif Nyholm:** Writing – review & editing, Supervision. **E. Kristofer Gamstedt:** Writing – review & editing, Supervision. **Ulf Jansson:** Funding acquisition, Conceptualization, Writing – original draft, Supervision.

Declaration of Competing Interest

The authors declare the following financial interests/personal relationships which may be considered as potential competing interests: Ulf Jansson reports financial support was provided by Sweden's Innovation Agency.

Data Availability

The data supporting the findings in this study are available from the corresponding author upon request.

Acknowledgments

We wish to thank Petter Ström for the assistance with ERDA measurements, which were performed at the Tandem laboratory at Uppsala University. We acknowledge Myfab Uppsala for providing facilities and experimental support. Myfab is funded by the Swedish Research Council (2019-00207) as a national research infrastructure. This study was performed in the framework of the competence center FunMat-II which is financially supported by VINNOVA (grant no 2016-05156).

Appendix A. Supporting information

Supplementary data associated with this article can be found in the

online version at [doi:10.1016/j.mtcomm.2023.107389](https://doi.org/10.1016/j.mtcomm.2023.107389).

References

- [1] U. Jansson, E. Lewin, Sputter deposition of transition-metal carbide films - a critical review from a chemical perspective, *Thin Solid Films* 536 (2013) 1–24, <https://doi.org/10.1016/j.tsf.2013.02.019>.
- [2] K. Lukaszewicz, Review of nanocomposite thin films and coatings deposited by PVD and CVD technology, in: M.M. Rahman (Ed.), *Nanomaterials*, InTech, Rijeka, 2011, pp. 145–162.
- [3] S. Zhang, D. Sun, Y. Fu, H. Du, Toughening of hard nanostructural thin films: a critical review, *Surf. Coat. Technol.* 198 (2005) 2–8, <https://doi.org/10.1016/j.surfcoat.2004.10.020>.
- [4] P. Ettmayer, W. Lengauer, *Carbides: transition metal solid state chemistry*, in: R. B. King (Ed.), *Encycl. Inorg. Chem.*, 3rd ed., Oxford University Press, 1994.
- [5] A.A. Voevodin, J.S. Zabinski, Load-adaptive crystalline-amorphous nanocomposites, *J. Mater. Sci.* 33 (1998) 319–327.
- [6] N. Nedfors, O. Tengstrand, E. Lewin, A. Furlan, P. Eklund, L. Hultman, U. Jansson, Structural, mechanical and electrical-contact properties of nanocrystalline-NbC/amorphous-C coatings deposited by magnetron sputtering, *Surf. Coat. Technol.* 206 (2011) 354–359, <https://doi.org/10.1016/j.surfcoat.2011.07.021>.
- [7] A. Furlan, J. Lu, L. Hultman, U. Jansson, M. Magnuson, Crystallization characteristics and chemical bonding properties of nickel carbide thin film nanocomposites, *J. Phys. Condens. Matter* 26 (2014), 415501, <https://doi.org/10.1088/0953-8984/26/41/415501>.
- [8] A. Furlan, U. Jansson, J. Lu, L. Hultman, M. Magnuson, Structure and bonding in amorphous iron carbide thin films, *J. Phys. Condens. Matter* 27 (2015) 1, <https://doi.org/10.1088/0953-8984/27/4/045002>.
- [9] M. Andersson, J. Höglström, S. Urbonaite, A. Furlan, L. Nyholm, U. Jansson, Deposition and characterization of magnetron sputtered amorphous Cr-C films, *Vacuum* 86 (2012) 1408–1416, <https://doi.org/10.1016/j.vacuum.2012.01.021>.
- [10] B. Trindade, M.T. Vieira, Modification of the structural order of transition metal-carbon systems by the addition of a Group VIII element, *Mater. Sci. Eng. A* 352 (2003) 195–201, [https://doi.org/10.1016/S0921-5093\(02\)00865-1](https://doi.org/10.1016/S0921-5093(02)00865-1).
- [11] U. Jansson, E. Lewin, M. Räsander, O. Eriksson, B. André, U. Wiklund, Design of carbide-based nanocomposite thin films by selective alloying, *Surf. Coat. Technol.* 206 (2011) 583–590, <https://doi.org/10.1016/j.surfcoat.2010.06.017>.
- [12] S. Zhang, X.L. Bui, J. Jiang, X. Li, Microstructure and tribological properties of magnetron sputtered nc-TiC/a-C nanocomposite, *Surf. Coat. Technol.* 198 (2005) 206–211, <https://doi.org/10.1016/J.SURFCOAT.2004.10.041>.
- [13] W. Yan, Y. Zhang, L. Chen, J. Luo, P. Pang, X. Zhang, B. Liao, M. Ying, Corrosion behavior and interfacial conductivity of amorphous hydrogenated carbon and titanium carbide composite (a-C:H/TiC) films prepared on titanium bipolar plates in PEMFCs, *Diam. Relat. Mater.* 120 (2021), 108628, <https://doi.org/10.1016/J.DIAMOND.2021.108628>.
- [14] J. Höglström, M. Andersson, U. Jansson, F. Björefors, L. Nyholm, On the evaluation of corrosion resistances of amorphous chromium-carbon thin-films, *Electrochim. Acta* 122 (2014) 224–233, <https://doi.org/10.1016/j.electacta.2013.11.130>.
- [15] A.S. Gago, S.A. Ansar, B. Saruhan, U. Schulz, P. Lettenmeier, N.A. Cañas, P. Gazdzicki, T. Morawietz, R. Hiesgen, J. Arnold, K.A. Friedrich, Protective coatings on stainless steel bipolar plates for proton exchange membrane (PEM) electrolyzers, *J. Power Sources* 307 (2016) 815–825, <https://doi.org/10.1016/J.JPOWSOUR.2015.12.071>.
- [16] U. Jansson, E. Lewin, Carbon-containing multi-component thin films, *Thin Solid Films* 688 (2019), 137411, <https://doi.org/10.1016/j.tsf.2019.137411>.
- [17] M. Braic, M. Balaceanu, A. Vladescu, C.N. Zotta, V. Braic, Deposition and characterization of multi-principal-element (CuSiTiZr)C coatings, *Appl. Surf. Sci.* 284 (2013) 671–678, <https://doi.org/10.1016/J.APSUSC.2013.07.152>.
- [18] V. Braic, A.C. Parau, I. Pana, M. Braic, M. Balaceanu, Effects of substrate temperature and carbon content on the structure and properties of (CrCuNbTiY)C multicomponent coatings, *Surf. Coat. Technol.* 258 (2014) 996–1005, <https://doi.org/10.1016/J.SURFCOAT.2014.07.044>.
- [19] H. Luo, S. Zou, Y.H. Chen, Z. Li, C. Du, X. Li, Influence of carbon on the corrosion behaviour of interstitial equiatomic CoCrFeMnNi high-entropy alloys in a chlorinated concrete solution, *Corros. Sci.* 163 (2020), 108287, <https://doi.org/10.1016/j.corsci.2019.108287>.
- [20] J. Chen, Z. Yao, X. Wang, Y. Lu, X. Wang, Y. Liu, X. Fan, Effect of C content on microstructure and tensile properties of as-cast CoCrFeMnNi high entropy alloy, *Mater. Chem. Phys.* 210 (2018) 136–145, <https://doi.org/10.1016/j.matchemphys.2017.08.011>.
- [21] L. Yang, C. Liu, M. Wen, X. Dai, Y. Zhang, X. Chen, K. Zhang, Small atoms as reinforced agent for both hardness and toughness of Group-VIB transition metal films, *J. Alloy. Compd.* 735 (2018) 1105–1110, <https://doi.org/10.1016/j.jallcom.2017.11.208>.
- [22] L. Zendejas Medina, M.V. Tavares da Costa, E.M. Paschalidou, G. Lindwall, L. Riekehr, M. Korvela, S. Fritze, S. Kolozsvári, E.K. Gamstedt, L. Nyholm, U. Jansson, Enhancing corrosion resistance, hardness, and crack resistance in magnetron sputtered high entropy CoCrFeMnNi coatings by adding carbon, *Mater. Des.* 205 (2021), 109711, <https://doi.org/10.1016/j.matdes.2021.109711>.
- [23] T. Suszko, W. Gulbiński, J. Morgiel, G. Greczynski, E. Dobruchowska, P. Dłuzewski, J. Lu, L. Hultman, Amorphous FeCrNi/a-C:H coatings with self-organized nanotubular structure, *Scr. Mater.* 136 (2017) 24–28, <https://doi.org/10.1016/j.scriptamat.2017.03.040>.

- [24] C. Zhang, M.C. Gao, CALPHAD modeling of high-entropy alloys, in: High-Entropy Alloy. Fundam. Appl., Springer International Publishing, 2016, pp. 399–444, https://doi.org/10.1007/978-3-319-27013-5_12.
- [25] H.L. Chen, H. Mao, Q. Chen, Database development and Calphad calculations for high entropy alloys: challenges, strategies, and tips, *Mater. Chem. Phys.* 210 (2018) 279–290, <https://doi.org/10.1016/j.matchemphys.2017.07.082>.
- [26] T.-C. Software, TCHEA3: TCS High Entropy Alloy Database, 2018. (https://www.thermocalc.com/media/35873/tchea3_extended_info.pdf) (Accessed 16 December 2019).
- [27] F. de la Peña, E. Prestat, V.T. Fauske, P. Burdet, J. Lähnemann, P. Jokubauskas, T. Furnival, M. Nord, T. Ostasevicius, K.E. MacArthur, D.N. Johnstone, M. Sarahan, J. Taillon, T. Aarholt, pquinn-dls, V. Migunov, A. Eljarrat, J. Caron, C. Francis, T. Nemoto, T. Poon, S. Mazzucco, actions-user, N. Tappy, N. Cautaearts, S. Somnath, T. Slater, M. Walls, F. Winkler, H.W. Ánes, hyperspy/hyperspy: Release v1.7.2, 2022. (<https://doi.org/10.5281/ZENODO.7090040>).
- [28] P. Ström, D. Primetzhofer, Ion beam tools for nondestructive in-situ and in-operando composition analysis and modification of materials at the Tandem Laboratory in Uppsala, *J. Instrum.* 17 (2022) P04011, <https://doi.org/10.1088/1748-0221/17/04/P04011>.
- [29] P. Ström, P. Petersson, M. Rubel, G. Possnert, A combined segmented anode gas ionization chamber and time-of-flight detector for heavy ion elastic recoil detection analysis, *Rev. Sci. Instrum.* 87 (2016), 103303, <https://doi.org/10.1063/1.4963709/368409>.
- [30] W.C. Oliver, G.M. Pharr, An improved technique for determining hardness and elastic modulus using load and displacement sensing indentation experiments, *J. Mater. Res.* 7 (1992) 1564–1583, <https://doi.org/10.1557/JMR.1992.1564>.
- [31] M.V. Tavares da Costa, J. Bolinsson, R.C. Neagu, P. Fayet, E.K. Gamstedt, Experimental assessment of micromechanical models for fragmentation analysis of thin metal oxide coatings on polymer films under uniaxial tensile deformation, *Surf. Coat. Technol.* 370 (2019) 374–383, <https://doi.org/10.1016/j.surfcoat.2019.03.035>.
- [32] J.E. Saal, I.S. Berglund, J.T. Sebastian, P.K. Liaw, G.B. Olson, Equilibrium high entropy alloy phase stability from experiments and thermodynamic modeling, *Scr. Mater.* 146 (2018) 5–8, <https://doi.org/10.1016/j.scriptamat.2017.10.027>.
- [33] M. Pourbaix, Atlas of electrochemical equilibria in aqueous solutions, NACE Int. Cebelcor (1974).
- [34] K.W. Chan, S.C. Tjong, Effect of secondary phase precipitation on the corrosion behavior of duplex stainless steels, *Materials* 7 (2014) 5268–5304, <https://doi.org/10.3390/ma7075268>.
- [35] M.C. Tropicovsky, J.R. Morris, P.R.C. Kent, A.R. Lupini, G.M. Stocks, Criteria for predicting the formation of single-phase high-entropy alloys, *Phys. Rev. X* 5 (2015) 1–6, <https://doi.org/10.1103/PhysRevX.5.011041>.
- [36] J.H. Kim, S. Kang, J.W. Park, E.D. Park, Y.K. Jun, J.Y. Han, J.H. Jung, N. Kim, G. H. Lee, Tailored hydrogen-free carbon films by tuning the sp²/sp³ Configuration, *ACS Appl. Electron. Mater.* 3 (2021) 1771–1779, https://doi.org/10.1021/ACSAPM.1C00046/ASSET/IMAGES/LARGE/EL1C00046_0008.JPEG.
- [37] J.F. Moulder, W.F. Stickle, P.E. Sobol, K.D. Bomben, Handbook of X-ray photoelectron spectroscopy, Physical Electronics, Inc., Eden Prairie, Minnesota, 1995. (<https://doi.org/10.1002/sia.740030412>).
- [38] J.C. Lascovich, R. Giorgi, S. Scaglione, Evaluation of the sp²/sp³ ratio in amorphous carbon structure by XPS and XAES, *Appl. Surf. Sci.* 47 (1991) 17–21, [https://doi.org/10.1016/0169-4332\(91\)90098-5](https://doi.org/10.1016/0169-4332(91)90098-5).
- [39] H.Y. Dai, Y.Q. Wang, X.R. Cheng, C.Y. Zhan, N.K. Huang, Characterization and properties of amorphous carbon coatings prepared by middle frequency pulsed unbalanced magnetron sputtering at different substrate bias, *Appl. Surf. Sci.* 258 (2012) 5462–5466, <https://doi.org/10.1016/j.apsusc.2012.02.039>.
- [40] G. Greczynski, D. Primetzhofer, L. Hultman, Reference binding energies of transition metal carbides by core-level x-ray photoelectron spectroscopy free from Ar⁺ etching artefacts, *Appl. Surf. Sci.* 436 (2018) 102–110, <https://doi.org/10.1016/J.APSUSC.2017.11.264>.
- [41] G. Panzner, W. Diekmann, The bonding state of carbon segregated to α -iron surfaces and on iron carbide surfaces studied by electron spectroscopy, *Surf. Sci.* 160 (1985) 253–270, [https://doi.org/10.1016/0039-6028\(85\)91040-4](https://doi.org/10.1016/0039-6028(85)91040-4).
- [42] A.L. Greer, Y.Q. Cheng, E. Ma, Shear bands in metallic glasses, *Mater. Sci. Eng. R. Rep.* 74 (2013) 71–132, <https://doi.org/10.1016/j.mser.2013.04.001>.
- [43] J.C. Halpin, J.L. Kardos, The Halpin-Tsai equations: a review, *Polym. Eng. Sci.* 16 (1976) 334–352, <https://doi.org/10.1002/pen.760160512>.
- [44] H.S. Myung, Y.S. Park, M.J. Jung, B. Hong, J.G. Han, Synthesis and mechanical properties of amorphous carbon films by closed-field unbalanced magnetron sputtering, *Mater. Lett.* 58 (2004) 1513–1516, <https://doi.org/10.1016/J.MATLET.2003.10.021>.
- [45] G. Hinds, E. Brightman, Towards more representative test methods for corrosion resistance of PEMFC metallic bipolar plates, *Int. J. Hydrogen Energy* 40 (2015) 2785–2791, <https://doi.org/10.1016/J.IJHYDENE.2014.12.085>.
- [46] E.M. Paschalidou, R. Lindblad, L.Z. Medina, D. Karlsson, U. Jansson, L. Nyholm, Corrosion studies on multicomponent CoCrFeMnNi(C) thin films in acidic environments, *Electrochim. Acta* 404 (2022), 139756, <https://doi.org/10.1016/j.electacta.2021.139756>.
- [47] F. Maillard, W. O. Silva, L. Castanheira, L. Dubau, F.H.B. Lima, Carbon corrosion in proton-exchange membrane fuel cells: spectrometric evidence for Pt-catalysed decarboxylation at anode-relevant potentials, *ChemPhysChem* 20 (2019) 3106–3111, <https://doi.org/10.1002/cphc.201900505>.